1 | **Revision 2**

2

3 Quantification of CO_2 concentration in apatite

4 KATHRYN CLARK[1], YOUXUE ZHANG[1*], FABIAN U. NAAB[2]

5 [1]Department of Earth and Environmental Sciences, University of Michigan, Ann Arbor, Michigan 48109, USA
6 [2]Department of Nuclear Engineering and Radiological Sciences, University of Michigan, Ann Arbor, Michigan 48109, USA

7

8

9

10 **ABSTRACT**

11

12   We have calibrated the infrared (IR) method for determining CO_2 concentrations in

13 apatite with absolute concentrations obtained through Nuclear Reaction Analysis (NRA). IR

14 data were obtained on double-polished apatite wafers using polarized transmission IR

15 spectroscopy. Due to the various sites and orientations of CO_3^{2-} in apatite, the IR spectra are

16 complicated and do not have the same shape in different apatite samples. Hence, simple peak

17 heights are not used to characterize CO_2 concentrations in apatite. The total absorbance (A_{total})

18 was derived using the integrated area under the curves in a given polarized spectral region. Then

19 A_{total} is calculated as $A_{E//c} + 2A_{E\perp c}$. The calibration has been carried out for two wavenumber

20 regions, one with high sensitivity and the other applicable to apatite with high CO_2

21 concentrations. The first calibration is for the fundamental asymmetric CO_3^{2-} stretching at

22 wavenumbers of 1600-1300 cm^{-1}, and the CO_2 concentration in ppm can be obtained as (0.0756

23 ±0.0036) A_{total}/d where d is sample thickness in cm. The fundamental stretching bands are strong

24 and hence sensitive for measuring low CO_2 concentrations in apatite, down to ppm level. The

25 second calibration is for the CO_3^{2-} bands at wavenumbers of 2650-2350 cm^{-1}, and the CO_2

* Email: youxue@umich.edu

1

26   concentration in ppm is (9.3±0.6) A_{total}/d where d is sample thickness in cm. These bands are

27   weak and hence are useful for measuring high CO_2 concentrations in apatite without preparation

28   of super-thin wafers. The anisotropy is significant. The difference between $A_{E//c}$ and $A_{E\perp c}$ can

29   reach a factor of 2.8. Hence, for high-accuracy, it is best to use polarized IR to determine CO_2

30   concentrations in apatite. For rough estimation, unpolarized IR spectra may be used by

31   estimating $A_{total} = 3A_{unpol}$, where A_{unpol} is the integrated absorbance from unpolarized spectra.

32

33   Keywords: Carbonate in apatite, IR spectroscopy, nuclear reaction analysis, NRA

34

35   **INTRODUCTION**

36

37   The mineral apatite is a common biomineral and is also an accessory mineral found in

38   terrestrial, martian and lunar rocks (e.g., McCubbin and Nekvasil 2008; Boyce et al. 2010;

39   McCubbin et al. 2010a, 2010b, 2012). It has the ability to take numerous elements, including

40   most volatile elements, into its structure, depending on the composition of the surrounding

41   milieu (Elliott 1994; Pan and Fleet 2002; Hughes and Rakovan 2015). The formula of apatite is

42    $M_5(ZO_4)_3X$, in which the M site is dominated by Ca^{2+}, but can also contain Sr^{2+}, Ba^{2+}, Pb^{2+}, Na^+,

43   and light rare earth elements. The Z site is dominantly P^{5+}, but can also contain As^{5+}, Si^{4+}, C^{4+},

44   and S^{6+}, and the X site is a mixture of F^-, OH^-, Cl^-, and/or CO_3^{2-}. Because of this, apatite serves

45   as a good indicator of the conditions of the magmatic environment, especially volatile

46   conditions, from which it forms (Webster and Piccoli 2015). In particular, CO_2 concentration in

47   apatite may be able to indicate the CO_2 concentration or fugacity in terrestrial-lunar-martian

48   magmas and metamorphic rocks. For this potential to be realized, it is essential to analyze CO_2

49   concentrations in small apatite crystals as well as zoning of CO_2 in apatite. The focus of this

50   study is on the quantification of CO_2 concentrations in apatite by Fourier transform infrared

51   spectroscopy (FTIR).

52   CO_2 enters the apatite structure as the carbonate ion CO_3^{2-} in a number of ways, resulting

53   in a series of complicated infrared (IR) peaks originating from CO_3^{2-} in apatite (Elliott 1994; Pan

54   and Fleet 2002; Tacker 2008). The CO_3^{2-} ion is a triangular plane ion, and may substitute into

55   two different sites in apatite: the OH^- ion site and the PO_4^{3-} site. The former is referred to as the

56   A site and the latter is referred to the B site for carbonate substitution (Fleet and Liu 2003; Fleet

57   and Liu 2007; Fleet 2009). In the OH^- site, CO_3^{2-} may be oriented such that the bisector of the

58   triangular CO_3^{2-} ion is parallel to the **c**-axis of apatite (called type A1), or such that the bisector

59   is perpendicular to the **c**-axis (called type A2) (Tacker 2008). Based on IR spectra, Tacker

60   (2008) also identified two different sites of CO_3^{2-} ion in B site, and interpreted them to be due to

61   alignment of the 3 oxygens of CO_3^{2-} onto oxygens of the different triangular faces of the PO_4^{3-}

62   tetrahedron (see also Ivanova et al. 2001). Charge balance can be achieved in a number of ways,

63   such as one CO_3^{2-} substituting for two OH^-, or CO_3^{2-} plus Na^+ substituting for PO_4^{3-} plus Ca^{2+},

64   etc. Each of these different substitutions results in slight changes in the apatite structure as well

65   as shifts in both the Raman and the IR bands. In addition, these substitutions are not mutually

66   exclusive, and often occur in combination within the same crystal. This multitudinous

67   substitution is most evident in the wavenumber region $1600 - 1300$ cm^{-1}. These substitutions are

68   so complex that the IR signal from a single crystal can elicit as many as 7 peaks in this region

69   (Tacker 2008).

70   There are a number of methods for assessing CO_2 concentrations in apatite (e.g.,

71   Gulbrandsen et al. 1966; Johnson and Maxwell 1981; Santos and Clayton 1995; Cassella et al.

3

72   2000; Marks et al. 2012; Grunenwald et al. 2014). Note that even though carbon in apatite is

73   present as the carbonate ion, the concentration here is conventionally referred to as the amount of

74   CO_2 (wt% or ppm) that would be released if apatite were heated up to release all the volatiles.

75   Previous methods are mostly the bulk method. These include total carbon titration or total CO_2

76   release (Santos and Clayton 1995; Grunenwald et al. 2014), FTIR spectra from a dispersion in a

77   KBr pellet (Santos and Clayton 1995; Marks et al. 2012; Grunenwald et al. 2014), and vapor

78   phase FTIR spectra obtained by reacting 50 mg of apatite with HCl (Cassella et al. 2000). These

79   methods typically require large samples, and even the most recent powder FTIR method by

80   Grunenwald et al. (2014) still requires milligrams of apatite. Apatite crystal specimens are not

81   always available in such large quantities. For example, in available lunar samples, apatite

82   crystals are often in the range of tens of micrometers in size (Boyce et al. 2010; McCubbin et al.

83   2010). In addition, the powder or vapor FTIR methods (Santos and Clayton 1995; Cassella et al.

84   2000; Marks et al. 2012; Grunenwald et al. 2014) are destructive and not enough for the

85   determination of heterogeneities at the 1000 μm scale. As demonstrated by Elliott (1994) and

86   Wang et al. (2011), polarized IR signals of OH and carbonate from single apatite crystals are

87   often very strong. Hence, the FTIR microbeam method on a single apatite crystals has a high

88   sensitivity and precision in determining the OH and carbonate concentrations once calibrated.

89   Elliott (1994) used polarized FTIR analyses to determine the structural setting and orientation of

90   the carbonate ion in apatite, whereas Wang et al. (2011) focused on polarized FTIR analyses of

91   H_2O concentrations.

92   In this work, we use polarized micro-FTIR to quantify CO_2 concentrations in apatite.

93   Although FTIR can be used to detect specific ion clusters (and specific sites and orientations) in

94   the crystal with high sensitivity and precision, conversion of the resulting peak intensities to

4

95   concentrations requires an absolute concentration technique for calibration. The creation of a

96   calibration curve, using large apatite crystals of varying concentrations, would allow for future

97   quantification of concentrations in smaller samples (Wang et al. 2011). Nuclear Reaction

98   Analysis (NRA) is an effective way to determine the absolute concentrations of carbonate in

99   large crystals (Mathez et al. 1987; Cherniak et al. 2010). The purpose of this project was to

100   compare FTIR data with NRA quantification of carbonate in apatite from a variety of sources in

101   order to build a calibration curve for the FTIR signatures in these crystals. However, one

102   difficulty in using single crystal FTIR to quantify CO_2 concentrations in apatite is that the

103   fundamental absorption bands are often too strong so that sometimes wafers, which are

104   impractically too thin, must be prepared. To overcome this difficulty, appropriate combination

105   bands that are orders of magnitude weaker can be used to determine CO_2 concentrations in

106   apatite when the concentration is relatively high.

107   In addition to the high sensitivity and precision, another advantage of using polarized

108   FTIR, and assessing spectra when the **E**-vector is parallel or perpendicular to the **c**-axis of the

109   crystal, is the improved accuracy in quantification of concentrations as well as revealing

110   structural information (Libowitzky and Rossman 1996). It is interesting that with all the

111   discussion of the importance of the alignment of the CO_3 ion with the **c**-axis of the apatite crystal

112   (Fleet and Liu 2003; Fleet et al. 2004; Tacker 2008; Fleet 2009), IR analysis of apatite parallel

113   and perpendicular to the **c**-axis is quite rare (Elliott 1994; Suetsugu et al. 1998). Because of the

114   different orientations of the carbonate ion, it is likely that the use of polarized FTIR will provide

115   greater detail regarding the variety of substitutions, with some more prevalent when **E**//**c**, and

116   others more prevalent when **E**⊥**c**, as well as more accurate quantification of CO_2 concentrations

117   in apatite.

5

118

119   **METHODS**
120

121 **Samples**

122   Four apatite samples were obtained from various locations: Durango, Mexico (Cerro);

123 High Atlas Mountains, Morocco (HAM); Faraday Township, Ontario (ROM); and one from an

124 unknown location purchased from an online vendor (GEM). The Durango apatite has been

125 extensively studied and is often used as a reference material (e.g., Young et al. 1969; McDowell

126 et al. 2005). Two of these samples (Cerro, HAM) were characterized in our laboratory by

127 electron microprobe (Henderson 2011) and used to calibrate the IR method to analyze H_2O

128 concentrations (Wang et al. 2011). Apatite from the same ROM sample batch (Royal Ontario

129 Museum No. M14821) was studied by Gulbrandsen et al. (1966). The compositions of the

130 apatite single crystals, as determined by electron microprobe by Henderson (2011) for Cerro and

131 HAM and in this study for ROM and GEM, are reported in Table 1. All the apatite crystals used

132 are fluorapatite with $F/(F+OH+Cl) > 0.7$, with Ca dominating the M site ($\geq$ 98% of the M site), P

133 dominating the Z site ($\geq$ 96% of the Z site), and all other elements (e.g., S, Si, Mg, Sr, Ba, REE,

134 and Cl) totaling less than 3 wt%.

135   All samples were mounted on glass slides with crystal bond and cut parallel to the **c**-axis

136 with a diamond wafering saw. Cerro and HAM are high-quality gem crystals with a euhedral

137 shape and were easy to cut into oriented wafers. The ROM and GEM crystals were more

138 difficult to mount and cut into oriented wafers because the original crystal surfaces are not

139 obvious. ROM was cut from a triangular prism crystal. GEM was originally nearly spherical so

140 the resulting wafer was an oval with a long diameter of 5.2 mm and a short diameter of 3.1 mm.

141 The accuracy of the orientation of the wafers was checked by polarized OH spectra (see below).

142   These samples were further cut into 2 pieces. One piece was used for NRA analysis and the

143   other was used for polarized micro-FTIR. For each of ROM and GEM, another section was

144   prepared for electron microprobe analyses.

145

146   **Electron Microprobe**

147   The electron microprobe analyses for two polished apatite crystal wafers (ROM and

148   GEM) followed the procedure of Henderson (2011). As discovered by Stormer et al. (1993), the

149   F Kα intensity in apatite varies with time, especially when the analyzed section is perpendicular

150   to **c**-axis. Henderson (2011) showed that accurate analyses may be obtained by analyzing the

151   apatite section parallel to **c**-axis using a defocused or rastered beam of 5 to 10 μm in diameter.

152   We used a 10-μm defocused beam at 15 kV and 10 nA on the apatite (100) sections. Full

153   analyses conditions can be found in Henderson (2011).

154

155   **FTIR**

156   For FTIR, samples were doubly polished at least three separate times to thicknesses

157   ranging from 1.4 mm to 20 μm. Sample thickness was determined using a Mitutoyo digital

158   micrometer (with a precision of ±1 μm and an accuracy of ±2 μm). For samples with a thickness

159   <100 μm, interference fringes in the FTIR spectra were used to verify and determine the

160   thickness using the equation:

161

162                                $d = 1/(2n\Delta\omega),$ (1)

163

7

164   where d is the thickness of the sample, n is the refractive index, and $\Delta\omega$ is the period of the

165   interference fringes in terms of wavenumbers. A refractive index of 1.65 was used.

166   Polarized spectra were obtained for both **E//c** and **E⊥c** on the single wafer cut parallel to

167   the **c**-axis using a Perkin-Elmer Spectrum GX FTIR spectrometer at the University of Michigan

168   with a microscope attachment that was purged with N_2 gas. Spectra were acquired with a mid-IR

169   source, KBr beamsplitter, KRS-5 IR wire grid polarizer and a liquid nitrogen cooled MCT

170   detector. An aperture of 50 µm by 50 µm was used. Data were recorded from 7800-700 cm^{-1},

171   with a resolution of 1 cm^{-1}.

172   The orientation to the **c**-axis was verified in each sample using the spectra near the

173   wavenumber 3540 (OH peak), which is zero when **E⊥c** and maximal when **E//c** (Levitt and

174   Condrate 1970; Wang et al. 2011). The peaks in apatite attributed to CO_3^{2-} were compared with

175   polarized FTIR spectra of a double-polished crystal of calcite ($CaCO_3$).

176

177   **Nuclear Reaction Analysis (NRA)**

178   We used Nuclear Reaction Analysis (NRA) to determine absolute carbon concentrations

179   in apatite (Mathez et al. 1987; Proust et al. 1994; Cherniak et al. 2010). The nuclear reaction is

180    $^{12}C(d,p)^{13}C$ (i.e., $^{12}C + {}^{2}H \rightarrow {}^{13}C + {}^{1}H$) (Proust et al. 1994; Wang and Nastasi 2009; Csedreki et

181   al. 2014). A high-energy beam of deuteron (^2H) particles bombards the target material (polished

182   apatite crystal). As the particles go into the target, some ^2H particles react with the target nucleus

183   (^{12}C), converting the target nucleus to a new nucleus (^{13}C) and releasing a reaction product (^1H)

184   with a specific amount of energy. The released ^1H ion, with a different energy, is detected in the

185   NRA proton spectrum at different energy channels.

186   The samples prepared for NRA were polished with SiC sandpaper and 0.3 µm alumina

8

187   powder on cloth. Samples were about 50 mm^2 in area and 1-3 mm thick. All NRA measurements

188   were carried out at the Michigan Ion Beam Laboratory (MIBL) at the University of Michigan

189   with the 1.7 MV tandem accelerator. The deuteron beam energy was selected to be 1.31 MeV to

190   maximize the $^{12}C(d,p)^{13}C$ nuclear reaction cross section (Wang and Nastasi 2009; Csedreki et al.

191   2014) and hence the signal in the spectrum used to quantify the carbon concentration in the

192   sample. A Si charged-particle detector with 15 keV energy resolution was used to acquire the

193   spectrum. The detector was placed at a scattering angle of 135°. For the acquisition of the sample

194   spectra, a 17.7-μm thick Kapton ($H_{10}C_{22}N_2O_5$) foil was placed in front of the detector to filter out

195   backscattered deuterons of low energy (< 1.1 MeV). This allowed us to increase in the deuteron

196   current on the sample and decrease the acquisition times. The acquisition times were 500

197   seconds with a deuteron current on the sample of 130 nA. During the acquisition of the spectrum

198   the direction of the deuteron beam is normal to the sample surface. The depth of the apatite

199   sample being probed was estimated using the SIMNRA software (Mayer 1999) to be ~6 μm.

200   Atomic carbon concentration was determined through NRA spectrum modeling also

201   using the SIMNRA program (Mayer 1999). The NRA method is an absolute method and no

202   independent calibration is necessary. Nonetheless, we verified the procedure by analyzing a

203   calcite ($CaCO_3$), and obtaining a carbon concentration of 19.3±1.3 atomic%, which is in

204   agreement with the stoichiometric concentration of carbon of 20 atomic%.

205

206   **RESULTS**
207

208   The NRA spectra and modeling curves are shown in Fig. 1. The peak at 2980 keV

209   reflects surface carbon contamination and the data from 2600-2940 keV indicate carbon in the

210   interior of the crystal. There is significant background in the NRA spectra and the detection

211   limit of the NRA method is 0.113 wt% CO_2. Therefore, carbon concentration in some apatite

212   cannot be well resolved from NRA alone. For example, for Cerro, the NRA signal at 2600-2940

213   keV is indistinguishable from the background (Fig. 1). Hence, for Cerro, the fitting quality is

214   low and the uncertainty in modeling the carbon concentration is large. In order to determine

215   concentrations better, we used constraints from FTIR spectra, which have a high sensitivity to

216   estimate the background in NRA and subtract the same background counts from the NRA signals

217   for all samples. Based on IR spectra in the v3 region (see later sections), the integrated

218   absorbance A_{total} (see eq. (2)) for Cerro is ~1/5 of that for HAM. Because A_{total} is proportional to

219   the carbon concentration, we hence assigned a background to all the NRA spectra so that carbon

220   concentration in Cerro is ~1/5 of that for HAM. The resulting carbon concentration and error in

221   ROM, GEM, HAM, and Cerro are listed in Table 1. Note that the new error estimates reported

222   in Table 1 are achieved by combining the IR constraints of Cerro and HAM with the NRA data,

223   and are smaller than the error based on the NRA data alone. The CO_2 concentration in the ROM

224   apatite grain that we analyzed by NRA is 0.66 ± 0.06 wt% (1σ error) based on NRA analysis,

225   similar to the 0.57 wt% obtained by Gulbrandsen et al. (1966), who analyzed bulk apatite

226   crystals from the same location.

227   Typical IR spectra with the **E** vector parallel and perpendicular to the **c**-axis are shown in

228   Fig. 2. Band identifications were taken from Regnier et al. (1994) and Koleva and Petkova

229   (2012). The bands due to PO_4 at ~1000 cm^{-1} are typically oversaturated. Oversaturation is

230   indicated when the peak is at high absorbance values and when the peak region is not smooth,

231   but shows a lot of "noise". These data are not useable for quantification. The bands at ~2000

232   cm^{-1} are due to overtones of PO_4. The OH band at 3540 cm^{-1} is highly anisotropic, with zero

233   intensity when **E**⊥**c**, and is used to verify the orientation of the samples. The carbonate peaks in

10

234   apatite at higher wavenumbers can be assigned by comparison with assignments of peaks in

235   carbonate minerals (e.g., Gunasekaran et al. 2006) although the shapes of the carbonate peaks in

236   apatite are more complicated than in calcite and dolomite due to the lifting of the double

237   degeneracy and the multiple sites and orientations for the substitution of the CO_3 group into the

238   apatite structure. Following the assignments of Gunasekaran et al. (2006), the bands between

239   1700 and 1800 cm^{-1} are due to v1+v4, those between 2400 and 2600 cm^{-1} are due to 2v2+v4, and

240   those between 2800 and 2950 cm^{-1} are due to 2v3. The band at 1650 cm^{-1}, with a shoulder at

241   1620 cm^{-1}, does not change with the CO_2 or H_2O concentration, and appears to be due to a v3+v4

242   combination of PO_4^{3-}.

243   Among the fundamental carbonate vibrational modes, v3 (double-degenerate

244   antisymmetric stretch in the region of 1600–1300 cm^{-1}) is well separated from other bands and

245   hence well suited for the quantification of the CO_2 concentration. The v2 mode (out-of-plane

246   bend in the region of 850–900 cm^{-1}) is close to the main and oversaturated PO_4 bands, making it

247   difficult to use. There are numerous carbonate v3 and v2 bands in apatite due to different

248   carbonate substitution (A1, A2, B1, and B2, Tacker 2008). The v1 mode is IR-inactive and v4

249   (at ~720 cm^{-1}) is not always present. Hence, among the fundamental vibration modes, the v3

250   bands are calibrated in this study.

251   The v3 IR bands are strong and easily oversaturated. For our study, we specifically chose

252   some apatite with high CO_2 concentration because NRA requires high concentrations. Hence, to

253   avoid oversaturation of the IR bands, the samples had to be very thin, and the thinnest sample is

254   only 20 μm thick for ROM, which has the highest CO_2 concentration. That is, these IR bands

255   have high sensitivity and are good for obtaining low CO_2 concentrations in apatite once

256   calibrated but are not convenient for quantifying high CO_2 concentrations (e.g., $\geq$ 1000 ppm).

11

257   To overcome this difficulty, we also calibrated the combination bands for carbonate in apatite in

258   the region of 2650–2350 cm^{-1}. The bands in this region are about two orders of magnitude

259   weaker than those in 1600–1300 cm^{-1}, can only be clearly resolved when the samples are greater

260   than 0.5 mm thick (Fig. 3), and, hence, are well suited when the CO_2 concentration is high in

261   apatite. The use of combination bands to determine high species concentrations is similar to that

262   in studying H_2O in glasses (Newman et al. 1986).

263   To view the IR bands more clearly, the left 3 panels of Figure 3 illustrate the spectra in

264   the region of 1600–1300 cm^{-1} for the **E** vector parallel or perpendicular to the **c**-axis of the

265   apatite crystal. The shapes of the peaks are variable from one apatite crystal to another, with

266   major and minor peaks. For ROM and GEM apatite crystals, there are major double peaks at

267   1455 and 1428 cm^{-1}. When **E**⊥**c**, the two peaks are nearly identical, and when **E**//**c**, these peaks

268   become uneven in height. The spectra of ROM are similar to the polarized IR spectra of

269   francolite from Cornwall, England (Elliott 1994). The right 3 panels of Figure 3 show the same

270   information in the region of 2650–2350 cm^{-1}. Often the absorbance for **E**⊥**c** is larger than that

271   for **E**//**c**, but for Cerro, the opposite is true. It can be seen that the spectra shape in the region of

272   2650–2350 cm^{-1} is similar to that in the region of 1600–1300.

273   The shape of the spectra is related to the relative abundances of CO_3 groups in different

274   sites and orientations, and is variable for different apatite crystals (e.g., comparing ROM with

275   HAM). Therefore, the simple approach of using linear absorbance of main peaks (e.g., Wang et

276   al. 2011) would not work well, and we used the integrated absorbance over each region to

277   quantify the CO_2 concentration in apatite.

278

279   **Calibration**

12

280   The data in Table 1 are used to calibrate the FTIR technique for the analysis of CO_2

281   concentrations in apatite. The calibration is based on Beer's law describing the relationship

282   between the CO_2 concentration and the FTIR absorbance as:

283
284                                $C = \alpha A_{total}/d,$ (2)

285
286   where C is the CO_2 concentration, A_{total} $(= A_{E//c} + 2A_{E\perp c}$ because there are two principal axes that

287   are perpendicular to the **c**-axis and one that is parallel to the **c**-axis) is the total integrated

288   absorbance of the IR band in the wavenumber region of either 1600–1300 cm^{-1} or 2650–2350

289   cm^{-1}, with the total mean summation over three crystallographic directions; d is the sample

290   thickness; and α is a constant that contains the molar mass of CO_2, the density of apatite, and the

291   integrated molar absorptivity in a specific spectrum region. The unit of A_{total} is the same as that

292   of the wavenumber (cm^{-1}). The unit for d is chosen to be cm. The unit of C is chosen to be ppm

293   CO_2 ($C =1$ means 1 ppm CO_2). Hence, the unit of α is ppm·cm^2.

294   Because of the multiple possible peaks due to variations in the substitution of the CO_3^{2-}

295   ion (Regnier et al. 1994; Fleet and Liu 2004; Fleet et al. 2004), we used the integrated area

296   between the curve and the baseline as the characteristic to represent the CO_2 concentration in

297   apatite. To obtain the baseline, a regression line was created that formed a tangent across the

298   lowest point on either side of the bands defining the peaks in the wavenumber range (1600–1300

299   or 2650–2350 cm^{-1}) (Fig. 4). For the 1600–1300 cm^{-1} region, the lowest points are near 1580

300   cm^{-1} and 1360 cm^{-1} (with some variability), respectively. For the 2650–2350 cm^{-1} region, the

301   lowest points are near 2580 cm^{-1} and 2405 m^{-1}. Then the baseline was subtracted from the

302   spectrum. The total area of all the bands in a region between the two tangential points was

303   obtained by the numerical integration $\int Ad\omega$ from one tangential point to the other. This was

13

304   done for both the $\mathbf{E}\perp\mathbf{c}$ spectrum to obtain $A_{\mathbf{E}\perp\mathbf{c}}$ (the integrated absorbance for $\mathbf{E}\perp\mathbf{c}$), and for the

305   $\mathbf{E}//\mathbf{c}$ spectrum to obtain $A_{\mathbf{E}//\mathbf{c}}$ (the integrated absorbance for $\mathbf{E}//\mathbf{c}$). Then A_{total} was calculated as

306   $A_{\mathbf{E}//\mathbf{c}} + 2A_{\mathbf{E}\perp\mathbf{c}}$. The values of $A_{\mathbf{E}\perp\mathbf{c}}$, $A_{\mathbf{E}//\mathbf{c}}$, and A_{total} for all samples are listed in Table 1. For

307   convenience, the integrated absorbance in the 1600–1300 cm^{-1} region is referred to as A_{1440}, and

308   that in the 2650–2350 cm^{-1} region is referred to as A_{2500}. It can be seen that per sample

309   thickness, A_{total} in the 2650–2350 cm^{-1} region is about 0.8% of that in the 1300–1600 cm^{-1}

310   region.

311   Figure 5 illustrates the calibration curve for NRA (wt%) vs. the integrated area of the

312   FTIR signal at wavenumbers 1600–1300 cm^{-1} (a) and wavenumbers 2650–2350 cm^{-1} (b). The

313   data are fit by equation (2) (i.e., the intercept is forced to be zero) to obtain α using the York

314   algorithm (York 1969), but forcing the intercept to be zero. The Cerro sample is plotted but not

315   used in the fitting because it has already been used in estimating the background for NRA. For

316   the 1600-1300 cm^{-1} region (v3 bands), the fit value and 1σ error for the slope α (Fig. 5a) is:

317
318       $$\alpha_{1600\text{-}1300} = 0.0756\pm0.0036 \text{ ppm·cm}^2, \quad \text{MSWD} = 0.88. \qquad (2a)$$

319
320   For the 2650-2350 cm^{-1} region, the fit (Fig. 5b) gives:

321
322       $$\alpha_{2650\text{-}2350} = 9.3\pm0.6 \text{ ppm·cm}^2, \quad \text{MSWD} = 2.64. \qquad (2b)$$

323
324   The mean square weighted deviation (MSWD) is larger than 1, which probably reflects the

325   difficulty of integrating the smaller peaks over a wide range of wavenumbers.

326   On the basis of 2σ reproducibility of the IR spectra, the detection limit of the integrated

327   absorbance is on the order 1 cm^{-1}. Therefore, the detection limit for IR measurement of CO_2 in

328   apatite, using the v3 bands, can be sub-ppm for 1-mm thick apatite samples. For 0.1-mm thick

14

329   apatite crystals, the detection limit is about 8 ppm. That is, the v3 bands are very sensitive for

330   quantitative measurements of CO_2 in apatite using polarized IR on oriented crystals, but very

331   thin wafers must be prepared when the CO_2 concentration is > 0.1 wt%. On the other hand, for a

332   1-mm thick apatite crystal, the detection limit, using the bands in the 2650–2350 cm^{-1} region, is

333   about 100 ppm, and wt% level CO_2 concentrations can be measured using these bands.

334

335   **H_2O concentration in the apatite samples**

336   The IR data also provide information on the H_2O concentration using the calibration of

337   Wang et al. (2011). All the spectra show a dominant peak at 3540 cm^{-1} for OH in apatite, and

338   hence a simple linear absorbance can be used to obtain the H_2O concentration. For HAM and

339   Cerro, the peak at 3540 cm^{-1} was oversaturated (the samples were not thin enough for the OH

340   peak because no special effort was made to obtain OH concentrations). Wang et al. (2011)

341   reported H_2O concentrations of 0.44 and 0.085 wt% for HAM and Cerro, respectively. For

342   ROM and GEM, the H_2O concentrations obtained are shown in Table 1. It can be seen that

343   ROM has the lowest H_2O but the highest CO_2 concentration among the samples. The GEM

344   crystal used in this study has a lower H_2O concentration than the Gem3 and Gem4 crystals used

345   in Wang et al. (2011).

346

347   **DISCUSSION**

348

349   **The various peaks in the v3 region**

350   The substitution of CO_3^{2-} into the apatite crystal is complex (Elliott 1994; El Feki et al.

351   1999; Comodi and Liu 2000; Ivanova et al. 2001; Leventouri et al. 2001; Fleet and Liu 2003,

15

352   2004, 2005; Fleet et al. 2004; Antonakos et al. 2007; Koleva and Petkova 2012). As summarized

353   by Tacker (2008), CO_3^{2-} can substitute on the OH (or Cl or F) site (Type A) as well as on a PO_4^{3-}

354   site (Type B). Type A substitutions occur in two different forms (Fleet et al. 2004). Using X-ray

355   structural analysis, Fleet and Liu (2003) and Fleet et al. (2004) discovered an A-type substitution

356   ordered along the apatite channel, which they labeled A1 because they also identified a second

357   Type A substitution in a "stuffed" position, which may act as a charge balance for a B-type

358   substitution (A2). The different Type A substitutions are reflected by different bands in the IR

359   spectrum, with A1 bands at 1541 and 1449 cm^{-1} and A2 bands at 1563 and 1506 cm^{-1} (Fleet et al.

360   2004). The Type B substitutions also occur in two different forms. According to Tacker (2008),

361   the B1 substitution is on one face of the PO_4 ion, while the B2 substitution is on a different face

362   with resulting IR spectral bands at 1450 and 1409 cm^{-1} (B1) and 1460 and 1427 cm^{-1} (B2). One

363   benefit of using polished single crystals and polarized spectra is the ability to pull out the details

364   from these differing substitutions.

365   The utility of using polarized vectors parallel and perpendicular to the **c**-axis of the

366   crystal is evident in Figure 6. When **E**⊥**c**, the two major peaks are similar in height. When **E**//**c**,

367   the band at 1428 cm^{-1} is smaller in height relative to the band at 1455 cm^{-1}. This would imply

368   that the band at 1428 cm^{-1} (B2) is reflecting the activity of a substitution that is at a high angle to

369   the **c**-axis and thus decreases when the energy is parallel to **c**. The band at ~1406 cm^{-1} has been

370   identified as a B1 signal, which corresponds to v3a in Fleet et al. (2004), parallel to the **c**-axis.

371   There are other subtle differences between the perpendicular and parallel spectra, with small

372   shoulders appearing at the wavenumbers identified by Tacker (2008) as the four substitution

373   sites. For example, the A1 substitution is stronger at 1455 cm^{-1} (combined with the B2

374   substitution) and disappears at higher wavenumbers. The A1 substitution at these higher

16

375   wavenumbers is evident only when $\mathbf{E}//\mathbf{c}$. The A2 substitution is visible only when $\mathbf{E}\perp\mathbf{c}$, which is

376   consistent with integration in the columnar anion (F^-, Cl^-, OH^-) perpendicular to the $\mathbf{c}$-axis (Fleet

377   et al. 2004; Tacker 2008). The IR bands for the B1 and B2 substitutions are at lower

378   wavenumbers than those for the A1 and A2 substitutions.

379   In addition to being able to identify the multiple substitutions of CO_3^{2-} into apatite, which

380   is aided by the use of spectra from both parallel and perpendicular energy bands, the integrated

381   area of the entirety from these wavenumbers can be used to quantify the amount of CO_3^{2-} in the

382   crystal using a calibration curve. An implicit assumption is that all the subspecies have the same

383   integrated molar absorptivity. Note these are all subspecies of CO_3^{2-}, not chemically different

384   species, such as CO_3^{2-} and CO_2, or OH and H_2O. Even for major species of the same element,

385   the integrated molar absorptivities are similar. For example, Newman et al. (1986) estimated

386   that for two major species of H (hydroxyl group OH^- and neutral molecule H_2O) in rhyolitic

387   glasses, the integrated molar absorptivity for OH is 1.67 times that for H_2O at the 3550 cm^{-1}

388   band, and 0.83 times that for H_2O at the 4000 cm^{-1} band, and 1.16 times that for H_2O at the 7100

389   cm^{-1} band. On the other hand, Leschik et al. (2004) cautioned that it is difficult to verify whether

390   the results in Newman et al. (1986) are due to differences in the molar absorptivities or due to

391   structural variations, meaning that molar absorptivities of different H species may be roughly

392   identical. Furthermore, it is expected that the integrated molar absorptivities of differently

393   positioned or oriented CO_3^{2-} are more similar than the different chemical species of OH^- and

394   H_2O. Hence, the assumption, that the differently sited or oriented CO_3^{2-} subspecies have the

395   same integrated molar absorptivity, is reasonable. Considering that even the difference or

396   similarity of the molar absorptivities for major hydrous species, molecular H_2O, and hydroxyl

397   groups, is still not resolved, the resolution of possible small differences in the integrated molar

398   absorptivities for different CO_3^{2-} subspecies must await future work.

399   Once the various substitutions of CO_3^{2-} into apatite are understood and the peak positions

400   well quantified, it may be possible to deconvolute the various peaks in Figure 6 and use them to

401   quantify the concentrations of each type and subtype of CO_3^{2-} substitution in apatite (Comodi

402   and Liu 2000). The relative concentrations of the various subspecies may depend on

403   temperature, pressure, melt composition, (such as the availability of P and F-OH-Cl), and other

404   ambient conditions. If the controlling factors for the different substitutions are understood, the

405   deconvoluted concentrations of the CO_3^{2-} subspecies might be able to provide rich information

406   on apatite formation conditions.

407

408   **Using unpolarized spectra to roughly estimate CO_2 concentrations in apatite**

409   Because apatite is ubiquitous in both geological and biological systems, the use of these

410   calibrations may be widespread. One advantage of calibrating for both lower (1600-1300 cm^{-1})

411   and higher (2650-2450 cm^{-1}) wavenumbers is that samples with a higher carbonate content do

412   not have to be thinned to <100 μm in order to quantify the carbonate concentration.

413   Often apatite crystals are small or otherwise difficult to orient. For CO_3^{2-} in apatite, at

414   least for the four samples studied in this work, the degree of anisotropy is not very large, with the

415   ratio of $A_{//\mathbf{c}}/A_{\perp\mathbf{c}}$ ranging from 0.47 to 2.73 (i.e., of order 1) for the 1600–1300 cm^{-1} bands. This is

416   in contrast to the OH band at 3540 cm^{-1} in apatite, which is completely anisotropic, with the ratio

417   of $A_{//\mathbf{c}}/A_{\perp\mathbf{c}}$ approaching infinity. The smaller degree of anisotropy means that the CO_2

418   concentration in apatite may be roughly estimated using unpolarized spectra on unoriented

419   apatite crystals. Such rough estimation can be achieved by measuring a couple of unpolarized

18

420   spectra on random unoriented apatite sections, finding the average integrated absorbance,

421   multiplying it by 3 to estimate the total integrated absorbance (A_{total}), and then using eq. (2), and

422   the appropriate value of α, to estimate the CO_2 concentration. Consider the range of $A_{//\mathbf{c}}/A_{\perp\mathbf{c}}$

423   ratios to be from 0.47 to 2.73 as observed in this study for the 1600–1300 cm^{-1} bands. If the ratio

424   of $A_{//\mathbf{c}}/A_{\perp\mathbf{c}} = 0.47$, then using a single unpolarized spectrum of a random section would lead to an

425   estimated A_{total} to be 0.57 to 1.21 times that of the true A_{total}. If the ratio of $A_{//\mathbf{c}}/A_{\perp\mathbf{c}} = 2.73$, then

426   using a single unpolarized spectrum of a random section would lead to an estimated A_{total} to be

427   0.63 to 1.73 times that of the true A_{total}. Combining these results, the estimated A_{total} and CO_2

428   content would be 0.57 to 1.72 times the true values using one unpolarized IR spectrum on a

429   random section. Measuring and averaging two or more randomly oriented sections would reduce

430   the uncertainty significantly. Hence, using unpolarized IR spectra on random sections to

431   estimate CO_2 concentration is expected to produce acceptable results.

432

433   **IMPLICATIONS**

434

435   We have calibrated polarized IR spectra on oriented apatite sections for the quantitative

436   measurement of CO_2 concentrations in apatite, using absolute concentrations from nuclear

437   reaction analysis. Calibration was carried out on two sets of vibrational bands, one suitable for

438   low CO_2 concentrations and the other for high CO_2 concentrations. Polarized IR spectra on

439   oriented apatite sections not only provide a precise method to determine CO_2 concentrations in

440   apatite, but also contain rich details about carbonate substitutions in apatite. Such details have

441   the potential to elucidate the formation conditions. In addition, our data, using polarized IR

442   spectra, show that carbonate in apatite displays only a weak degree of anisotropy. Hence,

19

443   unpolarized IR spectra and KBr powder IR spectra may also be used to roughly estimate CO_2

444   concentrations in apatite.

445   The ability to measure CO_2 concentrations in apatite is the first step towards the

446   determination of the partition coefficient of CO_2 between apatite and various melts, and towards

447   the inference of the CO_2 concentration in the melt from which apatite formed.

448

459

460   **REFERENCES CITED**

461   Antonakos, A., Liarokapis, E. and Leventouri, T. (2007) Micro-Raman and FTIR studies of
462   synthetic and natural apatites. Biomaterials, 28, 3043-3054.

463   Boyce, J.W., Liu, Y., Rossman, G.R., Guan, Y., Eiler, J.M., Stolper, E.M. and Taylor, L.A.
464   (2010) Lunar apatite with terrestrial volatile abundances. Nature, 7305, 466-469.

465   Cassella, A., de Campos, R., Garrigues, S., de la Guardia, M. and Rossi, A. (2000) Fourier
466   transform infrared determination of CO_2 evolved from carbonate in carbonated apatites.
467   Fresenius Journal of Analytical Chemistry, 367, 556-561.

20

468   Cherniak, D.J., Hervig, R.L., Koepke, J., Zhang, Y., and Zhao, D. (2010) Analytical methods in
469   diffusion studies. Reviews in Mineralogy and Geochemistry, 72, 107-170.

470   Comodi, P. and Liu, Y. (2000) CO_3 substitution in apatite: further insight from new crystal-
471   chemical data of Kasekere (Uganda) apatite. European Journal of Mineralogy, 5, 965-974.

472   Csedreki, L., Uzonyi, I., Sziki, G.A., Szikszai, Z., Gyurky, G., and Kiss, A.Z. (2014)
473   Measurements and assessment of $^{12}C(d,p\gamma)^{13}C$ reaction cross sections in the deuteron energy
474   range 740-2000 keV for analytical applications. Nuclear Instruments and Methods in Physics
475   Research Section B: Beam Interactions with Materials and Atoms, 328, 59-64.

476   El Feki, H., Savariault, J.M. and Ben Salah, A. (1999) Structure refinements by the Rietveld
477   method of partially substituted hydroxyapatite: $Ca_9Na_{0.5}(PO_4)_{4.5}(CO_3)_{1.5}(OH)_2$. Journal of
478   Alloys and Compounds, 1-2, 114-120.

479   Elliott J.C. (1994) Structure and Chemistry of the Apatites and other Calcium Orthophosphates.
480   389 p. Elsevier, Amsterdam.

481   Fleet, M.E., and Liu, X.Y. (2003) Carbonate apatite type A synthesized at high pressure: new
482   space group (P-3) and orientation of channel carbonate ion. Journal of Solid State Chemistry,
483   174, 412-417.

484   Fleet, M.E., and Liu, X.Y. (2004) Location of type B carbonate ion in type A-B carbonate apatite
485   synthesized at high pressure. Journal of Solid State Chemistry, 177, 3174-3182.

486   Fleet, M.E. and Liu, X.Y. (2005) Local structure of channel ions in carbonate apatite.
487   Biomaterials, 36, 7548-7554.

488   Fleet, M., Liu, X. and King, P. (2004) Accommodation of the carbonate ion in apatite: An FTIR
489   and X-ray structure study of crystals synthesized at 2-4 GPa. American Mineralogist, 89,
490   1422-1432.

491   Fleet, M.E., and Liu, X. (2007) Coupled substitution of type A and B carbonate in sodium-
492   bearing apatite. Biomaterials, 28, 916-926.

493   Fleet, M.E. (2009) Infrared spectra of carbonate apatites: v(2)-Region bands. Biomaterials, 8,
494   1473-1481.

495   Grunenwald, A., Keyser, C., Sautereau, A.M., Crubezy, E., Ludes, B. and Drouet, C. (2014)
496   Revisiting carbonate quantification in apatite (bio)minerals: a validated FTIR methodology.
497   Journal of Archaeological Science, 49, 134-141.

498   Gulbrandsen, R.A., Kramer, J.R., Beatty, L.B., and Mays, R.E. (1966) Carbonate-bearing apatite
499   from Faraday Township, Ontario, Canada. American Mineralogist, 51, 819-824.

21

500   Gunasekaran, S., Anbalagan, G. and Pandi, S. (2006) Raman and infrares spectra of carbonates
501   of calcite structure. Journal of Raman Spectroscopy, 9, 892-899.

502   Henderson, C.E. (2011) Protocols and Pitfalls of Electron Microprobe Analysis of Apatite. Dept.
503   of Geol. Sci., MS thesis, p. 69. University of Michigan, Ann Arbor, MI.

504   Hughes, J.M. and Rakovan, J.F. (2015) Structurally robust, chemically diverse: Apatite and
505   apatite supergroup minerals. Elements, 3, 165-170.

506   Ivanova, T., Frank-Kamenetskaya, O., Kol'tsov, A. and Ugolkov, V. (2001) Crystal structure of
507   calcium-deficient carbonated hydroxyapatite. Thermal decomposition. Journal of Solid State
508   Chemistry, 2, 340-349.

509   Johnson, W.M., and Maxwell, J.A. (1981) Rock and Mineral Analysis. 506 p. Wiley & Sons,
510   New York.

511   Koleva, V. and Petkova, V. (2012) IR spectroscopic study of high energy activated Tunisian
512   phosphorite. Vibrational Spectroscopy, 58, 125-132.

513   Leschik, M., Heide, G., Frischat, G.H., Behrens, H., Wiedenbeck, M., Wagner, N., Heide, K.,
514   Geissler, H., and Reinholz, U. (2004) Determination of H_2O and D_2O contents in rhyolitic
515   glasses using KFT, NRA, EGA, IR spectroscopy, and SIMS. Phys. Chem. Glasses, 45, 238-
516   251.

517   Leventouri, T., Chakoumakos, B.C., Papanearchou, N. and Perdikatsis, V. (2001) Comparison of
518   crystal structure parameters of natural and synthetic apatites from neutron powder diffraction.
519   Journal of Materials Research, 9, 2600-2606.

520   Levitt, S.R., and Condrate Sr., R.A. (1970) The polarized infrared spectra of hydroxyl ion in
521   fluorapatite. Applied Spectroscopy, 24, 288-289.

522   Libowitzky, E. and Rossman, G. (1996) Principles of quantitative absorbance measurements in
523   anisotropic crystals. Physics and Chemistry of Minerals, 6, 319-327.

524   Marks, M.A.W., Wenzel, T., Whitehouse, M.J., Loose, M., Zack, T., Barth, M., Worgard, L.,
525   Krasz, V., Eby, G.N., Stosnach, H. and Markl, G. (2012) The volatile inventory (F, Cl, Br, S,
526   C) of magmatic apatite: An integrated analytical approach. Chemical Geology, 241-255.

527   Mathez, E., Blacic, J., Beery, J., Hollander, M. and Maggieore, C. (1987) Carbon in olivine -
528   results from Nuclear-Reaction Analysis. Journal of Geophysical Research, B5, 3500-3506.

529   Mayer, M. (1999) SIMNRA, a simulation program for the analysis of NRA, RBS and ERDA. In
530   Application of Accelerators in Research and Industry, Pts 1 and 2, vol. 475, p. 541-544. AIP
531   Conference Proceedings, American Institute of Physics, Melville, New York.

532   McCubbin, F.M. and Nekvasil, H. (2008) Maskelynite-hosted apatite in the Chassigny meteorite:
533   Insights into late-stage magmatic volatile evolution in martian magmas. American
534   Mineralogist, 4, 676-684.

535   McCubbin, F.M., Hauri, E.H., Elardo, S.M., Vander Kaaden, K.E., Wang, J. and Shearer,
536   C.K.,Jr. (2012) Hydrous melting of the martian mantle produced both depleted and enriched
537   shergottites. Geology, 8, 683-686.

538   McCubbin, F.M., Steele, A., Hauri, E.H., Nekvasil, H., Yamashita, S. and Hemley, R.J. (2010a)
539   Nominally hydrous magmatism on the Moon. Proceedings of the National Academy of
540   Sciences of the United States of America, 25, 11223-11228.

541   McCubbin, F.M., Steele, A., Nekvasil, H., Schnieders, A., Rose, T., Fries, M., Carpenter, P.K.
542   and Jolliff, B.L. (2010b) Detection of structurally bound hydroxyl in fluorapatite from
543   Apollo Mare basalt 15058,128 using TOF-SIMS. American Mineralogist, 8-9, 1141-1150.

544   Newman, S., Stolper, E.M., and Epstein, S. (1986) Measurement of water in rhyolitic glasses:
545   calibration of an infrared spectroscopic technique. American Mineralogist, 71, 1527-1541.

546   Pan, Y. and Fleet, M. (2002) Compositions of the apatite-group minerals: Substitution
547   mechanisms and controlling factors. Reviews in Mineralogy and Geochemistry, 48, 13-49.

548   Proust, C., Husson, E., Blondiaux, G. and Coutures, J.P. (1994) Residual Carbon Detection in
549   Barium-Titanate Ceramics by Nuclear-Reaction Technique. Journal of the European Ceramic
550   Society, 3, 215-219.

551   Regnier, P., Lasaga, A., Berner, R., Han, O. and Zilm, K. (1994) Mechanism of (CO_3)-O-2-
552   substitution in Carbonate-Fluorapatite - Evidence from FTIR spectroscopy, C-13 NMR, and
553   quantum-mechanical calculations. American Mineralogist, 9-10, 809-818.

554   Santos, R.V. and Clayton, R.N. (1995) The carbonate content in high-temperature apatite - an
555   analytical method applied to apatite from the Jacupiranga Alkaline Complex. American
556   Mineralogist, 3-4, 336-344.

557   Suetsugu, Y., Shimoya, I. and Tanaka, J. (1998) Configuration of carbonate ions in apatite
558   structure determined by polarized infrared spectroscopy. Journal of the American Ceramic
559   Society, 3, 746-748.

560   Tacker, R.C. (2008) Carbonate in igneous and metamorphic fluorapatite: Two type A and two
561   type B substitutions. American Mineralogist, 1, 168-176.

562   Wang, K.L., Zhang, Y. and Naab, F.U. (2011) Calibration for IR measurements of OH in apatite.
563   American Mineralogist, 8-9, 1392-1397.

564   Wang, Y. and Nastasi, M. (editors) (2009) Handbook of Modern Ion Beam Materials Analysis,
565   2nd Edition, Material Research Society.

23

566   Webster, J.D., and Piccoli, P.M. (2015) Magmatic apatite: a powerful, yet deceptive, mineral.
567   Elements, 11, 177-182.

568   York, D. (1969) Least-squares fitting of a straight line with correlated errors. Earth and Planetary
569   Science Letters, 5, 320-324.

570   Young, E.J., Myers, A.T., Munson, E.L., and Conklin, M.M. (1969) Mineralogy and
571   geochemistry of fluorapatite from Cerro de Mercado, Durango, Mexico. USGS Professional
572   Paper, 650-D, D84-D93.

573

574   Table 1. Chemical composition of apatite crystals used in this study
575

Sample	ROM	GEM	HAM	Cerro
# of analyses	*9*	*10*	*18*	*20*
P_2O_5	40.36(13)	40.27(54)	40.72(68)	41.04(68)
As_2O_5	0.04(2)	0.04(4)	0.01(2)	0.08(2)
SO_3	0.02(1)	1.09(5)	0.46(4)	0.44(4)
SiO_2	0.09(2)	0.41(3)	0.62(2)	0.32(2)
CaO	54.32(13)	54.50(29)	54.95(54)	54.22(53)
SrO	0.11(3)	0.11(2)	0.13(1)	0.09(1)
Na_2O	0.10(1)	0.30(3)	0.10(2)	0.28(2)
Y_2O_3	0.19(4)	0.00(3)	0.05(1)	0.09(1)
La_2O_3	0.08(8)	0.06(4)	0.25(2)	0.43(2)
Ce_2O_3	0.25(3)	0.15(4)	0.36(2)	0.62(2)
Pr_2O_3	0.04(2)	0.05(4)	0.02(3)	0.05(3)
Nd_2O_3	0.14(2)	0.07(3)	0.11(2)	0.18(2)
F	3.93(6)	2.83(6)	2.51(8)	3.40(9)
Cl	0.033(5)	0.04(1)	0.33(2)	0.46(2)
H_2O	0.043(8)	0.24(1)	0.44(1)	0.085(14)
CO_2	0.66(6)	0.18(4)	0.14(3)	0.03(1)
-O=F,Cl	*-1.66*	*-1.20*	*-1.13*	*-1.535*
Total	*98.74*	*99.15*	*100.072*	*100.35*
Number of ions normalized to M = the sum of mono-, di- & trivalent cations = 5				
P	*2.908*	*2.881*	*2.875*	*2.925*
S	*0.001*	*0.069*	*0.029*	*0.028*
Si	*0.008*	*0.034*	*0.052*	*0.028*
C	*0.077*	*0.021*	*0.016*	*0.003*
Ca	*4.953*	*4.935*	*4.950*	*4.898*
F	*1.057*	*0.756*	*0.696*	*0.922*
OH	*0.024*	*0.135*	*0.245*	*0.048*
Cl	*0.005*	*0.005*	*0.045*	*0.057*

576   Data for ROM and GEM are from this study, and data for HAM and Cerro are from Henderson (2011). V_2O_5,
577   Al_2O_3, FeO, MgO, MnO, PbO, BaO, K_2O, Sm_2O_3, Gd_2O_3, Dy_2O_3, ThO_2, and UO_2 are also measured for HAM and
578   Cerro, but their concentrations are at or below detection limit. H_2O and CO_2 concentrations are from IR (Wang et
579   al. 2011; this study).
580
581

25

582   Table 2. NRA and FTIR data on apatite from this study
583

Apatite	H_2O wt%	CO_2 wt%	A_{1440} $E\perp c$	A_{1440} $E//c$	A_{1440} total	A_{2500} $E\perp c$	A_{2500} $E//c$	A_{2500} total
ROM	0.043±0.008	0.664±0.055	37250	17380	91870	323±17	125±3	772±34
GEM	0.24±0.01	0.181±0.040	8890±52	6590±263	24380±159	64.5±1.3	27.5±0.7	157±3
HAM	--	0.142±0.034	5018±270	5438±134	15474±674	43.7±1.3	31.6±1.3	119.1±1.2
Cerro	--	0.028±0.012	683	1868	3234	--	--	--

584   Note: (1) H_2O concentration is based on IR measurement in this study using the calibration of Wang et al. (2011).
585   (2) CO_2 concentration is based on NRA analyses in this study, except for Cerro, for which the CO_2 concentration
586   was estimated using the relationship between total absorbance of Cerro and the total absorbance of HAM (see text).
587   Because of this, the CO_2 values of Cerro are not used in the calibration. (3) The absorbances are integrated
588   absorbances per cm thickness. For Cerro, the CO_2 concentration is low and hence A_{2500} cannot be determined well.
589

26
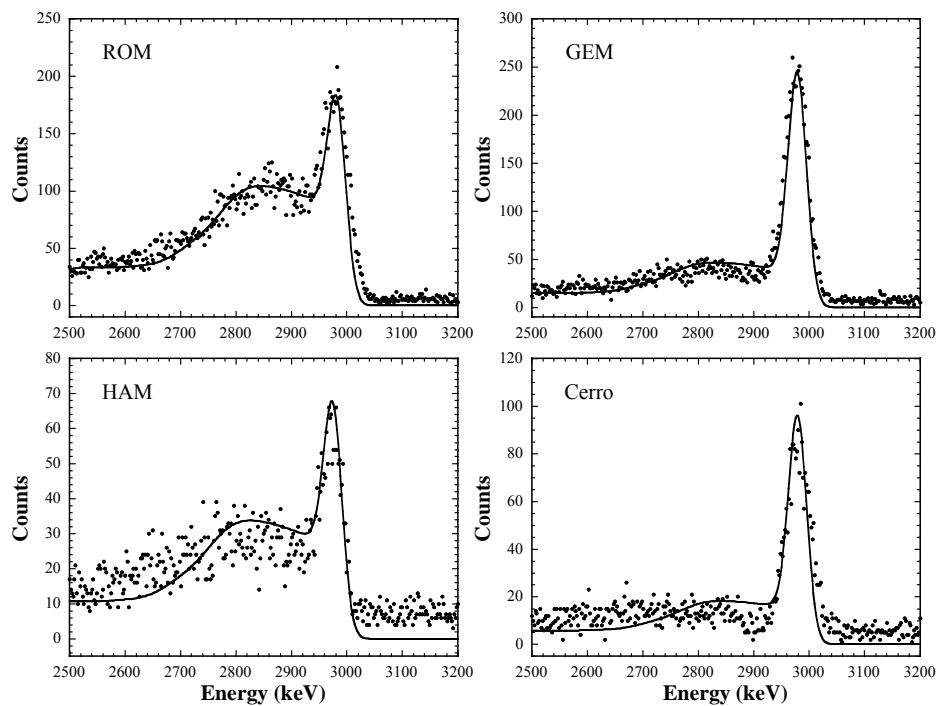
590
591
592   Fig. 1. NRA spectra of four samples. The points are data and the curves are modeling
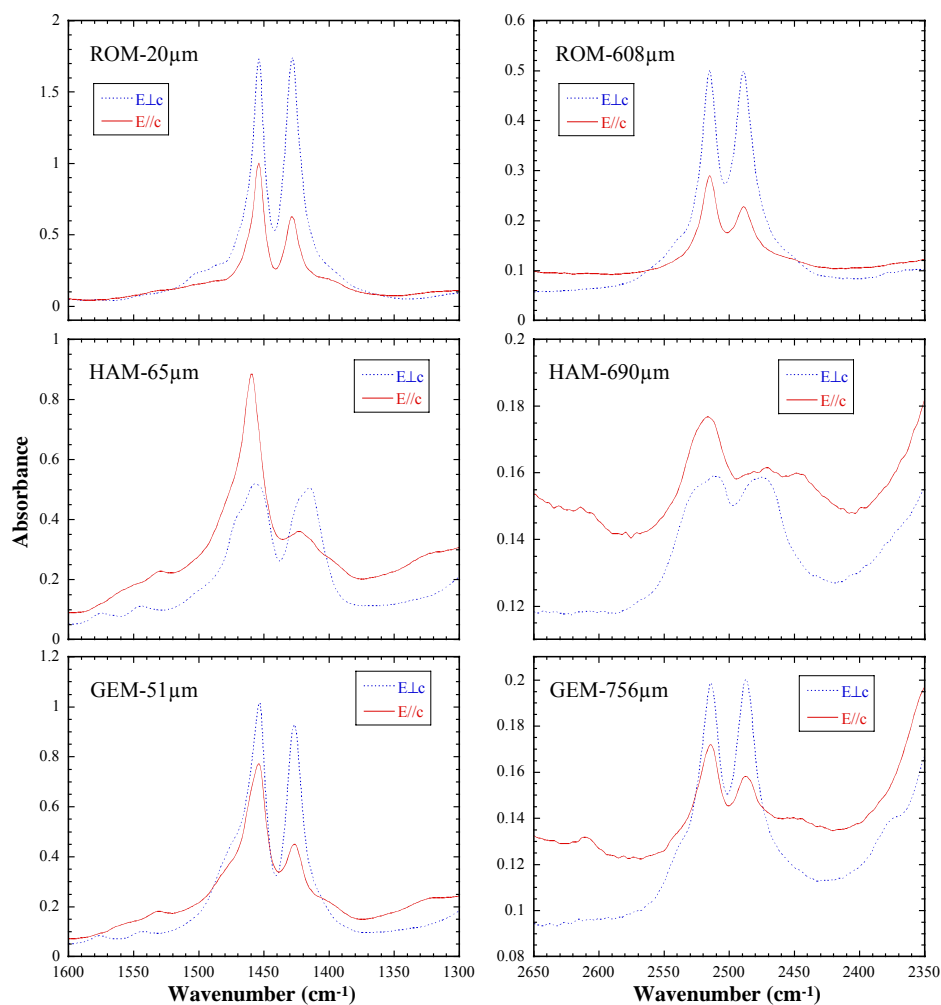593   of the data using the SIMNRA software (Mayer, 1999).
594

27

595
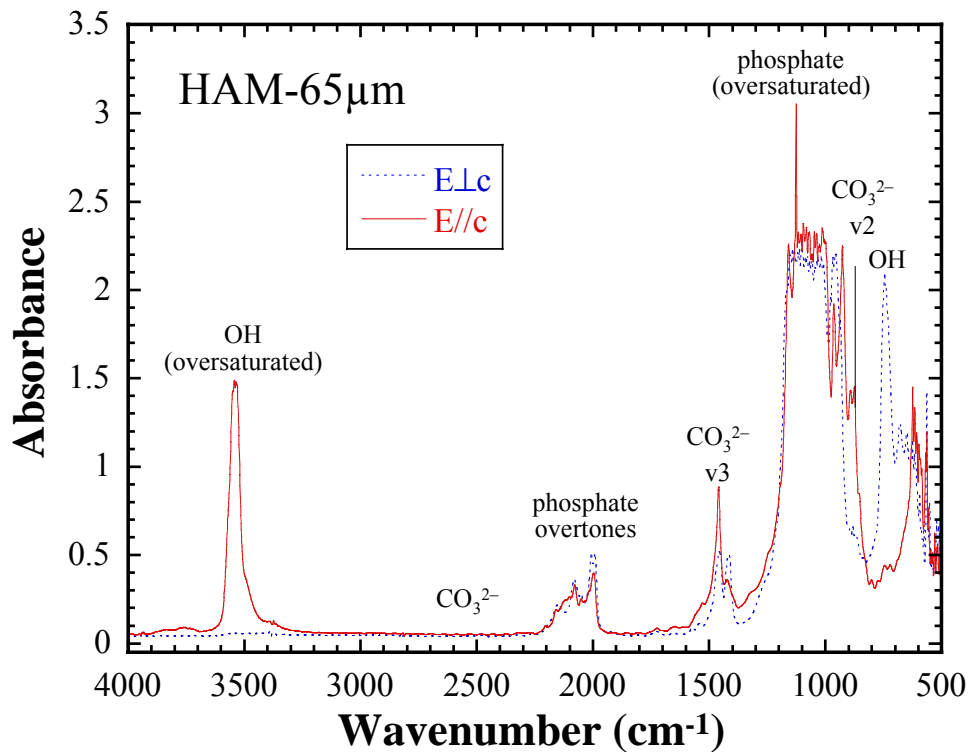
596
597
598   Fig. 2. Two polarized FTIR spectra for an apatite crystal from High Atlas Mountain (HAM),
599   one for **E⊥c** and one for **E//c**. The thickness of the crystal is 65 µm.
600

601

28

602

Figure 3. Polarized FTIR spectra at 1600–1300 cm^{-1} and 2650–2350 cm^{-1} collected from
single apatite crystals. Note the difference in this thickness of each sample, especially
between wavenumber region of 1600–1300 cm^{-1} and of 2650–2350 cm^{-1}. To avoid
oversaturation, the spectra at 1600–1300 cm^{-1} must be collected on very thin wafers. To get
significant signal, the spectra at 2650–2350 cm^{-1} must be collected on thick wafers. The
different shapes are due to different proportions of carbonate ions in A1, A2, B1, and B2
substitutions (see text).

610

29
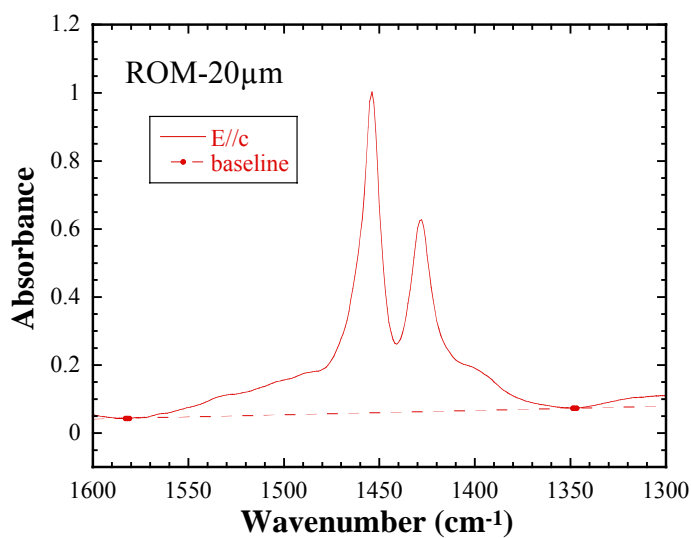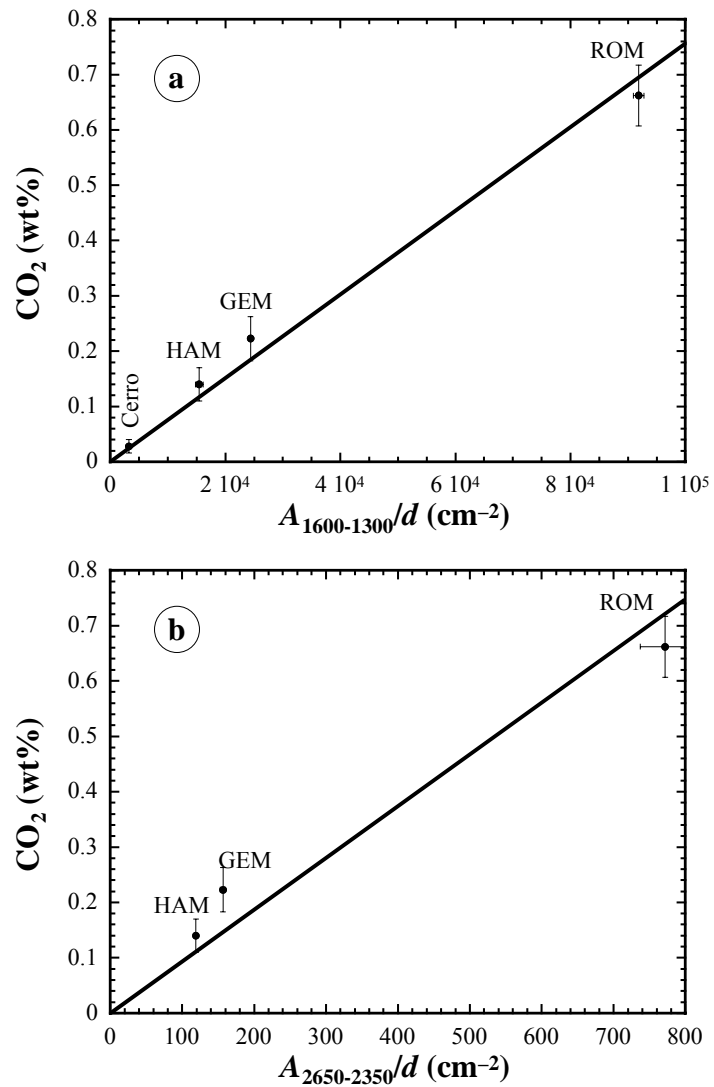
611

612 Figure 4. Illustration of baseline fitting for a polarized FTIR spectra at the v3 region (1600-1300
613 cm^{-1}) for **E**//**c** of a single apatite crystal ROM.

614

30

615

616 Figure 5. Calibration line for IR measurements of CO_2 in apatite. The integrated IR absorbances
617 are plotted on the horizontal axis. CO_2 concentrations determined by NRA are plotted on the
618 vertical axis. The Cerro sample is plotted but not used in the fitting because it has already been
619 used in estimating the background for NRA.

620

31

621
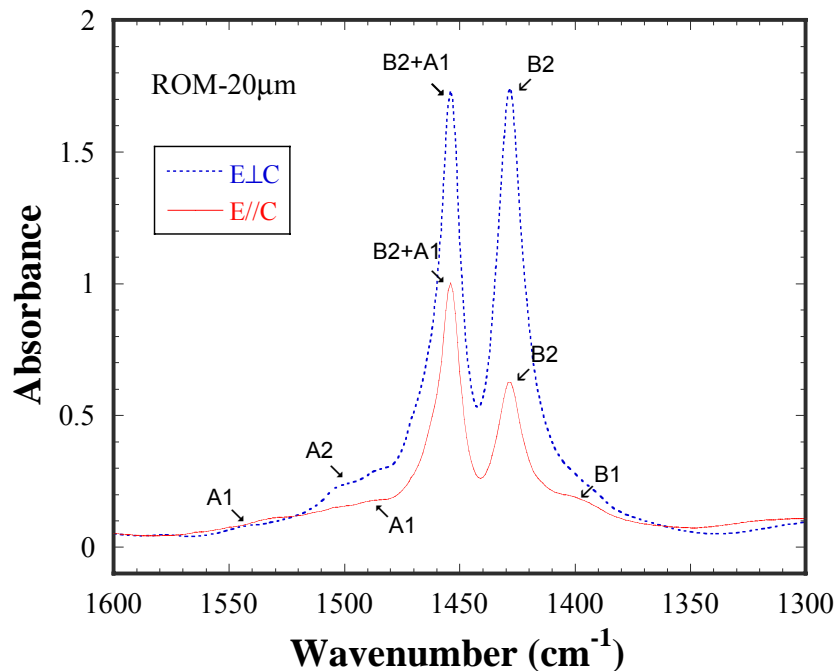
622

623   Figure 6. Polarized spectra illustrating the different peaks when **E⊥c** and when **E//c.** A1 is the
624   CO_2 substitution at the OH site and parallel to the c-axis of the crystal, A2 is perpendicular to the
625   c-axis. B1 and B2 substitutions are on different faces of the PO_4 ion (see text).
626